RESEARCH ARTICLE

NANO · MICRO small
www.small-journal.com

# Tunable Crystallinity and Electron Conduction in Wavy 2D Conjugated Metal–Organic Frameworks via Halogen Substitution

*Kamil Jastrzembski, Yingying Zhang, Yang Lu, Lukas Sporrer, Darius Pohl, Bernd Rellinghaus, Albrecht L. Waentig, Haojie Zhang, David Mücke, Shuai Fu, Miroslav Polozij, Xue Li, Jianjun Zhang, Mingchao Wang, Ahiud Morag, Minghao Yu, Aurelio Mateo-Alonso, Hai I. Wang, Mischa Bonn, Ute Kaiser, Thomas Heine, Renhao Dong,* and Xinliang Feng**

**Currently, most reported 2D conjugated metal–organic frameworks (2D c-MOFs) are based on planar polycyclic aromatic hydrocarbons (PAHs) with symmetrical functional groups, limiting the possibility of introducing additional substituents to fine-tune the crystallinity and electrical properties. Herein, a novel class of wavy 2D c-MOFs with highly substituted, core-twisted hexahydroxy-hexa-cata-benzocoronenes (HH-cHBCs) as ligands is reported. By tailoring the substitution of the c-HBC ligands with electron-withdrawing groups (EWGs), such as fluorine, chlorine, and bromine, it is demonstrated that the crystallinity and electrical conductivity at the molecular level can be tuned. The theoretical calculations demonstrate that F-substitution leads to a more reversible coordination bonding between HH-cHBCs and copper metal center, due to smaller atomic size and stronger electron-withdrawing effect. As a result, the achieved F-substituted 2D c-MOF exhibits superior crystallinity, comprising ribbon-like single crystals up to tens of micrometers in length. Moreover, the F-substituted 2D c-MOF displays higher electrical conductivity (two orders of magnitude) and higher charge carrier mobility (almost three times) than the Cl-substituted one. This work provides a new molecular design strategy for the development of wavy 2D c-MOFs and opens a new route for tailoring the coordination reversibility by ligand substitution toward increased crystallinity and superior electric conductivity.**

## 1. Introduction

2D conjugated metal–organic frameworks (2D c-MOFs) have attracted great attention,[1] due to the combination of the inherited advantages of traditional MOFs, such as intrinsic porosity, crystallinity, and abundant active sites, with electrical conductivity and tailorable bandgaps.[2–6] These properties make them excellent candidates for a variety of applications, such as optoelectronics, chemiresistive sensors,[7] batteries, supercapacitors,[7–10] and electrocatalysts.[11]

2D c-MOFs feature layer-stacked crystalline structures with strong in-plane conjugation and weak out-of-plane van der Waals interactions. A typical 2D c-MOF is usually constructed using benzene[12–16] as an organic building block or planar polycyclic aromatic hydrocarbons (PAHs), such as triphenylene,[17,18] coronene,[19] and phthalocyanine[20] which are substituted with symmetrical functional groups, such as —OH, —$NH_2$, —SH and —SeH.

K. Jastrzembski, Y. Zhang, Y. Lu, L. Sporrer, A. L. Waentig, S. Fu, M. Polozij, J. Zhang, M. Wang, A. Morag, M. Yu, T. Heine, R. Dong, X. Feng
Center for Advancing Electronics Dresden (CFAED) & Faculty of Chemistry and Food Chemistry
Technische Universität Dresden
Mommsenstrasse 4, 01062 Dresden, Germany
E-mail: renhaodong@sdu.edu.cn; xinliang.feng@tu-dresden.de
The ORCID identification number(s) for the author(s) of this article can be found under https://doi.org/10.1002/smll.202306732



**DOI: 10.1002/smll.202306732**

Y. Lu, H. Zhang, X. Feng
Max Planck Institute for Microstructure Physics
Weinberg 2, 06120 Halle (Saale), Germany

D. Pohl, B. Rellinghaus
Dresden Center for Nanoanalysis (DCN)
Technische Universität Dresden
Helmholtzstraße18, 01069 Dresden, Germany

D. Mücke, U. Kaiser
Central Facility of Materials Science Electron Microscopy
Universität Ulm
Albert-Einstein-, Allee 11, 89081 Ulm, Germany

However, these commonly used PAH ligands do not provide readily accessible sites for introducing functional substituents during their synthesis to fine-tune the resulting properties. Therefore, the introduction of functional substituents, especially electron-withdrawing groups (EWG), into the molecular backbone of the organic building block and their resulting impact on the corresponding MOF properties have so far not been investigated mainly due to the inherent limit on accessible sites. In this context, recent work showed that introducing electron-withdrawing hetero atoms (N) into the molecular backbone of the organic building block, triphenylene, to enhance the resulting crystallinity and electronic conductivity can be a viable strategy.[21] Moreover, the commonly used PAH ligands are all based on planar structures, and hence the impact of non-planar organic building blocks on the crystallinity and the charge transport properties is less unexplored.[22,23] In particular, the impact of wavy topological networks on the properties of the resulting 2D c-MOFs remains elusive.

In this work, we report the construction of wavy 2D c-MOFs via solution synthesis based on newly developed curved ligands, i.e., core-twisted 2,3,10,11,18,19-hexahydroxy-hexa-*cata*-benzocoronenes (HH-*c*HBCs) substituted by halogen groups, including 6,7,14,15,22,23-hexafluoro-2,3,10,11,18,19-hexahydroxy-*c*HBCs (HF-HH-*c*HBCs), 6,7,14,15,22,23-hexachloro-2,3,10,11,18,19-hexahydroxy-*c*HBCs (HCl-HH-*c*HBCs), and 6,7,14,15,22,23-hexabromo-2,3,10,11,18,19-hexahydroxy-*c*HBCs (HBr-HH-*c*HBCs). The uniqueness of these HX-HH-*c*HBCs (X = F, Cl, and Br) ligands can be attributed to their twisted and conformationally locked structure due to steric congestion between the hydrogens of the neighboring benzene rings, which prohibits molecular dynamics resulting in a structural rigid organic building block.[22,23] This molecular feature leads to a concave–convex self-complementary arrangement, resulting in the formation of 2D c-MOFs with wavy networks after coordination polymerization between HX-HH-*c*HBCs and metal centers (such as Cu). Although one might expect that the waviness might disturb the $\pi$–$\pi$-stacking arrangement and the overall crystallinity, our work demonstrates that the resultant $Cu_3$(HF-HH-*c*HBC)$_2$ 2D c-MOF powder exhibits high crystallinity comprising large ribbon-like crystals up to tens of micrometers in length, which can mainly be attributed to the smaller atomic size and strong electron-withdrawing effect of fluorine. In comparison, the chlorine- and bromine-substituents feature larger atomic sizes and weaker electron withdrawing effects rendering the resulting 2D-c-MOFs reduced crystallinity and electronic conductivity. Consequently, the $Cu_3$(HF-HH-*c*HBC)$_2$ 2D c-MOF exhibits a higher room-temperature electrical conductivity of $1.82 \times 10^{-2}$ S cm$^{-1}$ (two orders of magnitude) and higher charge mobility of $9.3 \pm 1.1$ cm$^2$/(Vs) (almost three times) than the chlorinated 2D-c-MOF $Cu_3$(HCl-HH-*c*HBC)$_2$. Our work develops a new family of wavy 2D c-MOFs and demonstrates an efficient strategy to tune the coordination bonding via the substitution of electron-withdrawing groups toward high crystallinity and superior electrical conduction.

## 2. Results and Discussion

### 2.1. Synthesis of Ligands and 2D c-MOFs

The c-HBC-ligands were synthesized through a three-step synthesis (**Figure 1**) according to a modified reported procedure[24] and numbered according to their differing substituents. In the first step, 1,3,5-tris(bromomethyl)benzene was reacted with 3,4-dimethoxyphenylboronic acid in a three-folded Suzuki coupling to afford 1,3,5-tris(3,4-dimethoxybenzyl)benzene (Tris-OMe-Mes (1)) with a yield of 52%. Next, the latter compound was transformed into the 6,7,14,15,22,23-hexafluoro-2,3,10,11,18,19-hexamethoxy-*c*HBC (HF-HM-*c*HBC) precursor through a coupling with 3,4-difluorobenzaldehyde in an aldol condensation reaction, followed by a Scholl reaction using the reagent $FeCl_3$ with a yield of 56%. The subsequent demethylation reaction using $BBr_3$ yielded the target compound HF-HH-*c*HBC with 85% yield. The synthesis of HCl-HH-*c*HBC and HBr-HH-*c*HBC followed the reaction procedure (synthetic details shown in Figures S1–S12, Supporting Information).

Next, we synthesized three 2D c-MOFs by coordination reaction between HX-HH-*c*HBCs (X = F, Cl, and Br and Cu(OAc)$_2$. Taking the synthesis of $Cu_3$(HF-HH-*c*HBC)$_2$ as an example, the HF-HH-*c*HBC ligand was dispersed in acetone and carefully injected on the top of an aqueous solution of Cu(OAc)$_2$. A metastable two-phase system was prepared and left for 48 h at room temperature. During the reaction, the two phases of water and acetone could be slowly merged into one phase, which slowed down the coordination polymerization, finally leading to the formation of the highly crystalline 2D c-MOF particles as precipitates with a high yield of 89% (details shown in Supporting Information). The successful coordination polymerization could be evidenced by Fourier-transform infrared spectroscopy (FT-IR) measurements, revealing the disappearance of the OH-stretching-frequencies at 3200, 3491, and 3235 cm$^{-1}$ arising from the ligands HF-, HCl-, HBr-HH-*c*HBC (Figures S13, S20, and S27, Supporting Information).

However, in contrast to the HF-HH-*c*HBC, no MOF precipitate could be observed when we followed the above-described reaction procedures for HCl-HH-*c*HBC- and HBr-HH-*c*HBC- ligands, demonstrating that the chlorinated and brominated ligands were much less reactive than the fluorinated one for the coordina-

S. Fu, H. I. Wang, M. Bonn
Max Planck Institute for Polymer Research
Ackermannweg 10, 55128 Mainz, Germany
M. Polozij, T. Heine
Institute of Resource Ecology
Helmholtz-Zentrum Dresden-Rossendorf, Leipzig Research, Branch
Bautzner Landstraße 400, 01328 Dresden, Germany
X. Li, R. Dong
Key Laboratory of Colloid and Interface Chemistry of the Ministry of Education
School of Chemistry and Chemical Engineering
Shandong University
27 Shandanan Road, Jinan 250100, China
A. Mateo-Alonso
POLYMAT
University of the Basque Country UPV/EHU
Avenida de Tolosa 72, Donostia-San Sebastian E- 20018, Spain
A. Mateo-Alonso
Basque Foundation for Science
Bilbao 48011, Spain

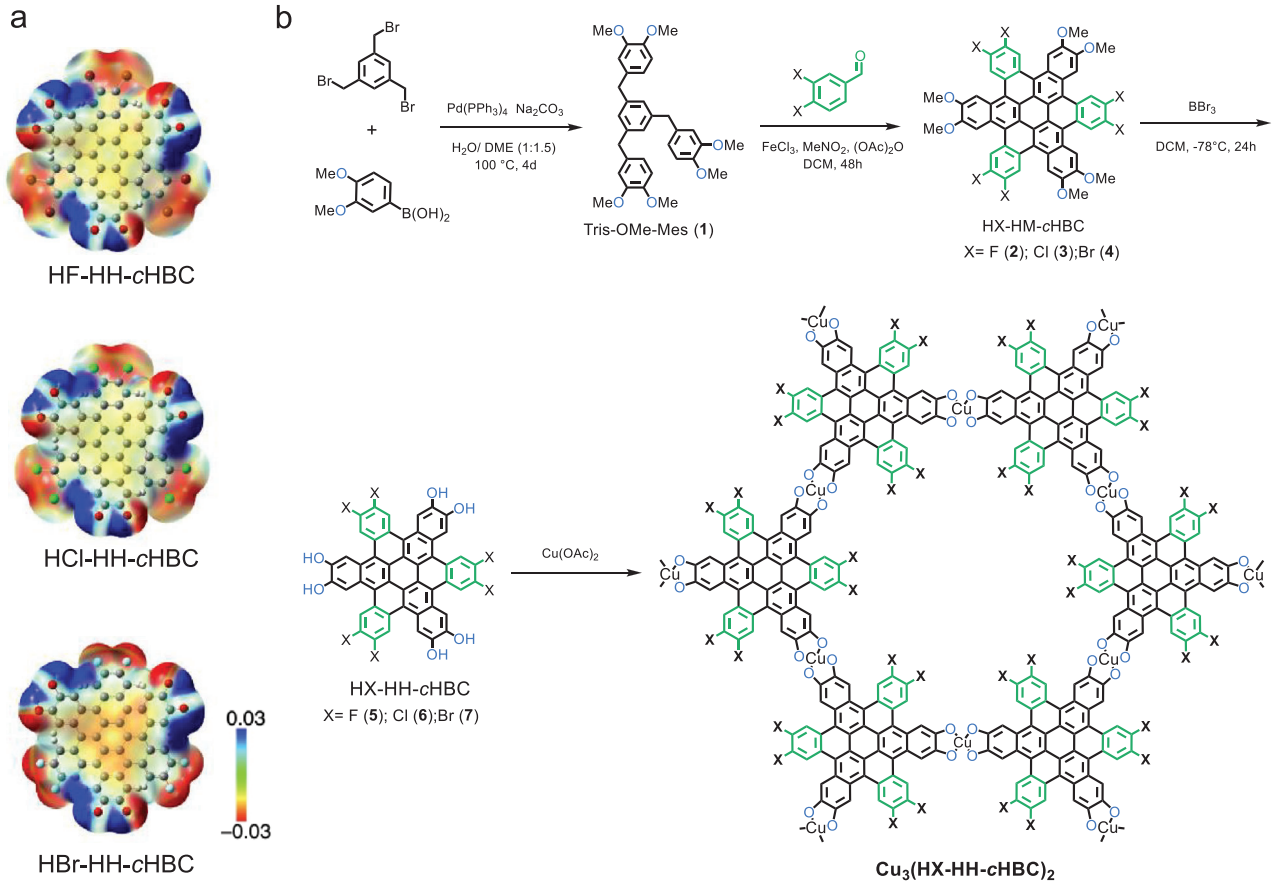


**Figure 1.** Design and synthesis of wavy 2D c-MOFs. a) Electrostatic potential maps (EPM) of the HF-, HCl-, and HBr-HH-*c*HBC ligands (from top to bottom), respectively, indicating that the electron core density is not significantly altered in comparison through the variation of the electron withdrawing substituents F, Cl, and Br. Color codes: red: electron-rich, blue: electron poor. b) Schematic illustration of the synthesis of *c*HBC ligands and wavy 2D c-MOFs.

tion reaction with Cu as the metal center. Therefore, a modified synthesis procedure with the further addition of ethylenediamine as a strong base, an extended reaction time of up to 4 days, and elevated temperatures (90 °C) was able to carry out the coordination reaction to obtain $Cu_3$(HCl-HH-cHBC)$_2$ with a yield of 53%. Similar reaction conditions to obtain the brominated MOF resulted only in amorphous MOF powders (details shown in Supporting Information).

### 2.2. Structural and Composition Characterization

The electron core density distributions were simulated with electrostatic potential maps (ESP) (Figure 1), indicating that all hydrogen atoms of the OH functional groups show a reduced electron density which translates into a reduced electron density at the metal binding site alike. A reduced electron density at the metal-binding site would lead to an increase in the acidity of the metal bond, making the in-plane bond formation more reversible and thus leading to an enhanced in-plane crystallinity.[21] The reduced electron density of the functional OH- group could additionally be confirmed experimentally with the chemical shifts of $^1$H- NMR spectroscopy, evidencing the decrease of the electron density of the OH- group according to the strength of the EWG in the order of F (9.95 ppm), Cl (9.86 ppm) and Br (9.81 ppm) (Figures S3, S7, and S11, Supporting Information), respectively. However, this downward trend was not observed in the electron density of the core of the c-HBC ligand, as indicated by $^1$H- and $^{13}$C- NMR of the remaining protons and carbons (Figures S3, S4, S7, S8, and S11, Supporting Information). According to our theoretical calculations of the highest occupied molecular orbitals (HOMO) and lowest unoccupied molecular orbitals (LUMO) (Figure S33, Supporting Information) of these three ligands, no systematic trend could be observed, as the EWGs were varied. Nevertheless, our characterizations demonstrate that $Cu_3$(HF-HH-cHBC)$_2$ displays the highest crystallinity (**Figures** 2a–c, and 3a) among the three obtained MOFs, which cannot be explained simply by the lowest electron core density. Rather, we suggest, that apart from the electron-withdrawing effect of fluorine, the more dominant factor for the comparably superior crystallinity of $Cu_3$(HF-HH-cHBC)$_2$ can be assigned to lesser steric hindrances originating from the actual atomic sizes of the substituents F (covalent radius: 60 pm), Cl (covalent radius: 102 pm) and Br (covalent radius: 120 pm).[25]

These significant differences in atomic size of the substituents affect the interlayer interaction and the subsequent layer stacking

 

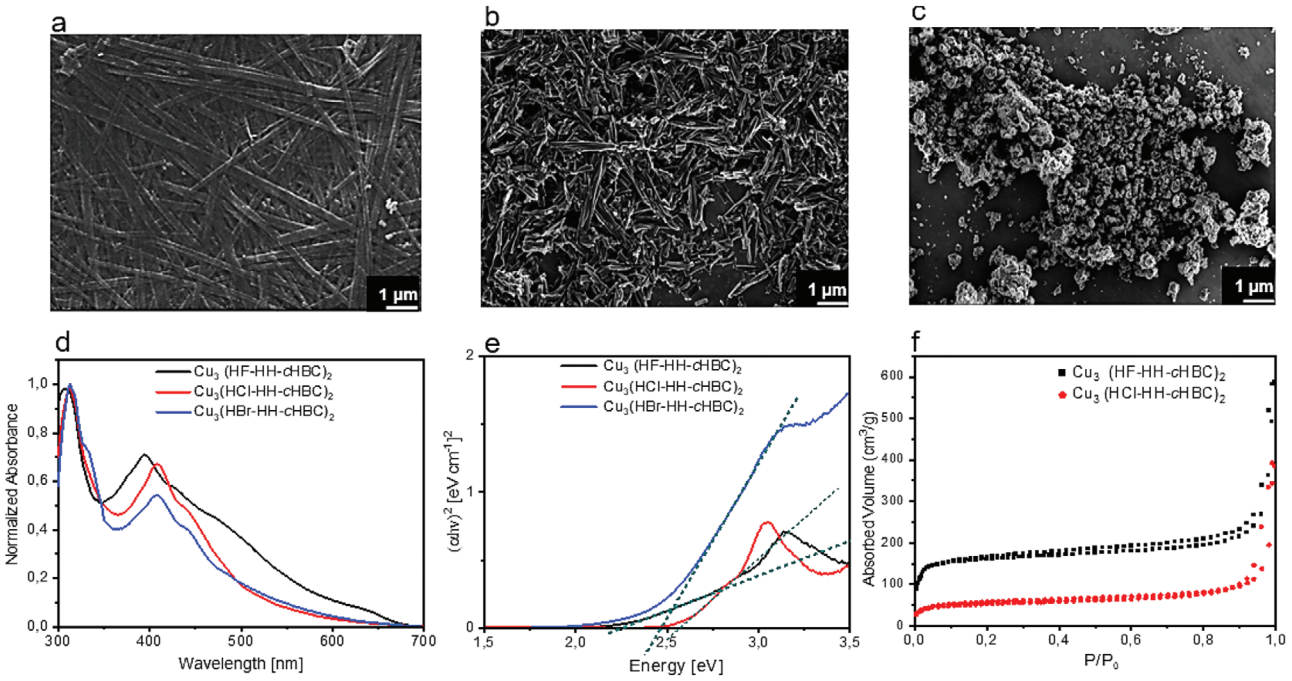


**Figure 2.** SEM, UV–vis, and BET measurements of the resultant wavy c-MOFs. ac) SEM images of $Cu_3$(HF-HH-*c*HBC)$_2$, $Cu_3$(HCl-HH-*c*HBC)$_2$, and $Cu_3$(HBr-HH-*c*HBC)$_2$. d) UV/vis absorption measurements indicate two absorption maxima for each 2D c-MOF: 304 and 396 nm for $Cu_3$(HF-HH-*c*HBC)$_2$, 313 and 407 nm for $Cu_3$(HCl-HH-*c*HBC)$_2$, 314 and 409 nm for $Cu_3$(HBr-HH-*c*HBC)$_2$. e) Optical bandgaps of $Cu_3$(HF-HH-*c*HBC)$_2$ (2.25 eV), $Cu_3$(HCl-HH-*c*HBC)$_2$ (2.56 eV), and $Cu_3$(HBr-HH-*c*HBC)$_2$ (2.50 eV) determined by the Tauc plot. f) Nitrogen adsorption/desorption isotherms of $Cu_3$(HF-HH-*c*HBC)$_2$ and $Cu_3$(HCl-HH-*c*HBC) indicating surface areas of 541 and 186 $m^2\ g^{-1}$, respectively.

along the c-axis leading to a stronger self-complementary preorganization for the perfect AA stacking and ordered arrangement along the out-of-plane direction for $Cu_3$(HF-HH-*c*HBC)$_2$ followed by $Cu_3$(HCl-HH-*c*HBC)$_2$ and $Cu_3$(HBr-HH-*c*HBC)$_2$. Accordingly, the morphology of $Cu_3$(HF-HH-*c*HBC)$_2$ followed the same trend (Figure 2a–c) evidenced by Scanning electron microscopy (SEM)- imaging. $Cu_3$(HF-HH-*c*HBC)$_2$ demonstrated highly homogenous distributed rod-like crystals with sizes of several micrometers (Figure 2a) and average widths of 200 nm resulting in high aspect ratios of 100–200. Comparably, $Cu_3$(HCl-HH-*c*HBC)$_2$ displayed a similar morphology but was less homogenously distributed and had smaller crystal lengths with an average of 1.0 micrometers (Figure 2b). $Cu_3$(HBr-HH-*c*HBC)$_2$, showed no distinct morphology and average crystal lengths of 200 nm (Figure 2c). These results demonstrate the significant impact of the substituents F, Cl, and Br on the resulting crystallinity (Figure 3a) and morphology of the corresponding 2D-c-MOFs.

The optical properties of all three MOFs were characterized by UV/Vis-spectroscopy (Figure 2d,e). All of them displayed two absorption maxima, the first one located in the UV range and the second one in the visible spectrum. Assignment of the absorption maxima indicated a blue shift of $Cu_3$(HF-HH-*c*HBC)$_2$ (304 and 396 nm) compared to $Cu_3$(HCl-HH-*c*HBC)$_2$ (313 and 407 nm) and $Cu_3$(HBr-HH-*c*HBC)$_2$ (314 and 409 nm). Although the blue shift of $Cu_3$(HF-HH-*c*HBC)$_2$ is quantitively small, it is to be expected due to the strong electron-withdrawing effect of the F-substituent. Analysis of the absorption spectra, using the Tauc-plot, resulted in direct optical bandgaps for $Cu_3$(HF-HH-*c*HBC)$_2$, $Cu_3$(HCl-HH-*c*HBC)$_2$ and $Cu_3$(HBr-HH-*c*HBC)$_2$ of 2.25, 2.56, and 2.45 eV, respectively. Remarkably, a comparison of the absorption maxima of the MOFs with their corresponding monomers showed very similar optical absorption patterns (Figures S13b, S20b, and S27b, Supporting Information).

The porous structures of all three 2D-c-MOFs were investigated through nitrogen adsorption/desorption isotherms (Figure 2f) at 77 K. In alignment with the crystallinity of the samples, $Cu_3$(HF-HH-*c*HBC)$_2$, showed the highest Brunauer-Emmett-Teller (BET) surface area of 541 $m^2\ g^{-1}$, $Cu_3$(HCl-HH-*c*HBC)$_2$, 186 $m^2\ g^{-1}$ whereas $Cu_3$(HBr-HH-*c*HBC)$_2$ showed no adsorption due to its amorphous structure. These results are consistent with the decreasing crystallinity from fluorinated to brominated MOF. The single pore size diameters were estimated as 1.9 nm using DFT models for all three MOFs. The experimental single pore size distribution of $Cu_3$(HF-HH-*c*HBC)$_2$, (Figure S18b, Supporting Information) showed a maximum at 1.8 nm, while $Cu_3$(HCl-HH-*c*HBC)$_2$, showed a maximum at 1.3 nm (Figure S25b, Supporting Information) which is slightly lower than its fluorinated counterpart. This discrepancy can be rationalized by taking the lower crystallinity and morphological homogeneity into account, as well as the slightly reduced accessibility of the pore volumes due to the increased atomic size of the Cl-substituents compared to the fluorinated ones.

Powder X-ray diffraction measurements (PXRD) measurements with Cu-K$\alpha$ radiation ($\lambda$ = 0.15 418 nm) demonstrated high crystallinity for $Cu_3$(HF-HH-*c*HBC)$_2$ with the most prominent reflexes at $2\theta$ = 3.72°, 6.35°, 7.22°, 12.52°, 14.40°, and 23.23° which refer to (100), (110), (200), (210), (300) and (001), respectively (Figure 3a). It should be noted that due to the

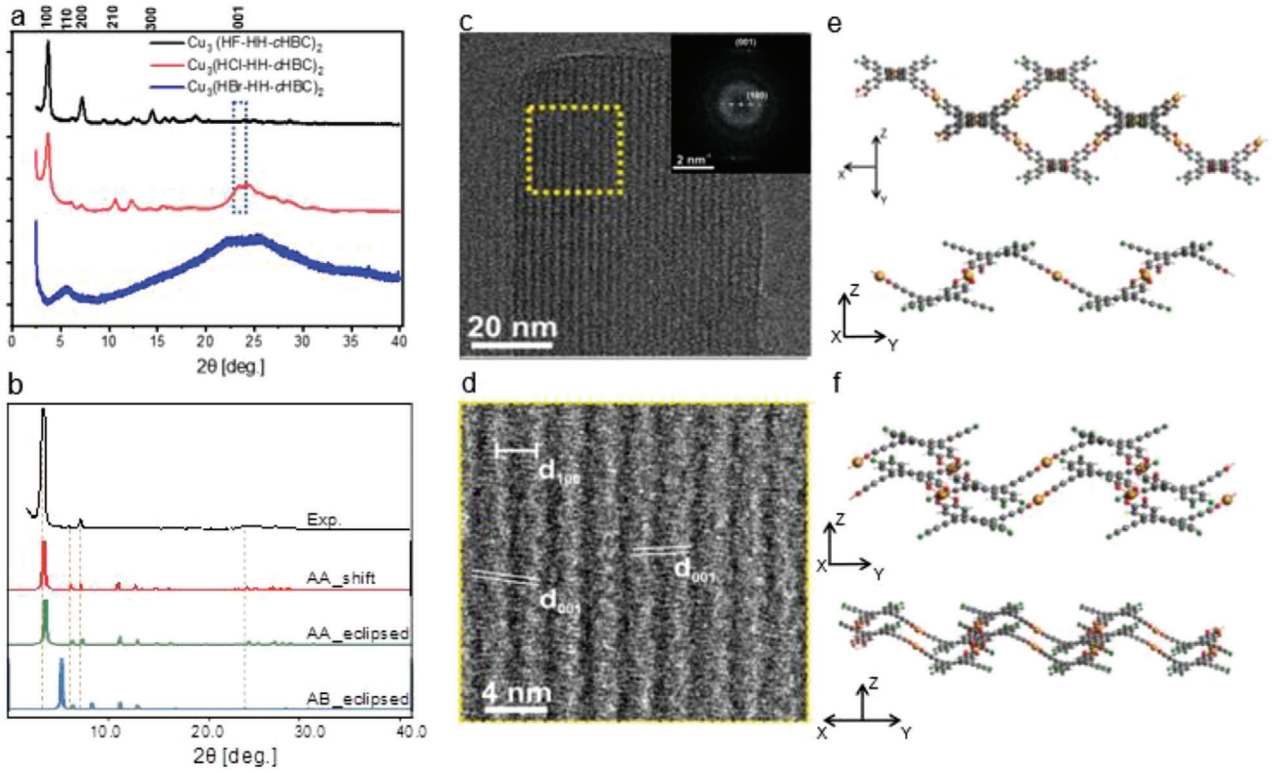


**Figure 3.** Structural characterization of wavy 2D c-MOFs. a) PXRD patterns of $Cu_3$(HF-HH-*c*HBC)$_2$, $Cu_3$(HCl-HH-*c*HBC)$_2$ and $Cu_3$(HBr-HH-*c*HBC)$_2$. b) Experimental and simulated PXRD patterns of $Cu_3$(HF-HH-*c*HBC)$_2$ suggesting the staggered AA stacking. c,d) HRTEM images of $Cu_3$(HF-HH-*c*HBC)$_2$ single crystal with (100) zone axis orientation. Inset: corresponding SAED pattern with the reflexes: $d_{100}$ = 2.38 nm, $d_{001}$ = 0.39 nm. e,f) Structural scheme of monolayer and AA-shift bilayer $Cu_3$(HF-HH-cHBC)$_2$, respectively. Black: carbon; white: hydrogen; green: fluorine; red: oxygen; yellow: copper.

high intensity of the (100) reflex, the (001) reflex is without a zoom-in difficult to spot for $Cu_3$(HF-HH-*c*HBC)$_2$ (Figure S14, Supporting Information). Similar reflexes were observed for $Cu_3$(HCl-HH-*c*HBC)$_2$, evidencing a similar crystalline structure. $Cu_3$(HBr-HH-*c*HBC)$_2$, on the other hand, displayed almost no distinguishable reflexes in alignment with its amorphous structure (Figure 3a; Figure S31, Supporting Information). HRTEM recordings (Figures 3c,d) of $Cu_3$(HF-HH-*c*HBC)$_2$ in [100] zone axis orientation demonstrate that the cHBC units adopted an edge-on configuration in the crystals. Analyzing the appearing reflections in the calculated Fast Fourier Transform (FFT), the (100)- and (001)- reflexes can be assigned. An additional zoom-in (Figure 3d) reveals the real space distribution of the $\pi-\pi$-stacking in (001) direction. Furthermore, the broad intensity distribution of the (001) reflection in the FFT (Figure 3c) indicates a wavy texture in (001) direction throughout the crystal.

Combining the experimental results (PXRD, HRTEM) with theoretical calculations (simulated PXRD and electronic properties calculation at PBE level26 in Figure 3b,d,f) enabled us to determine the crystal structure and the corresponding lattice parameters for the 2D c-MOFs $Cu_3$(HF-HH-*c*HBC)$_2$ that is linked through the oxygen–copper bonds forming a wavy structure. Each metal node is coordinated in a square planar arrangement by two neighboring HX-HH-*c*HBC ligands to form [$CuO_4$]-units, whereas each HX-HH-*c*HBC ligand is coordinated by three [$CuO_4$]- units according to its $C_3$- symmetry axis to arrange in a honeycomb structure. The resulting compounds can be described by the chemical compositional formula $Cu_3$(HX-HH-*c*HBC)$_2$ and the triclinic unit cell with the lattice parameters $a = b = 27.67$ Å, $c = 3.93$ Å, $\alpha = 89.22°$, $\beta = 90.55°$, $\gamma = 119.68°$. The predicted AA-shift and AA-eclipsed stacking pattern match the experimental PXRD results well (Figure 3b). Additionally, our calculations indicated an increased relative energy for the AA-eclipsed stacking structure of 33.76 kJ mol$^{-1}$, compared to the AA-shift stacking structure, confirming the correctness of the AA-shift stacking for the $Cu_3$(HX-HH-cHBC)$_2$ (X = F, Cl). The monolayer adopts a zig-zag alignment resulting in a wavy structure along the side view (Figure 3e).

The presence of all expected elements for each MOF could be proven, respectively, using X-ray photoelectron spectroscopy (XPS) (Figures S17, S24, and S30, Supporting Information). The analysis of the high-resolution spectrum of Cu for $Cu_3$(HF-HH-*c*HBC)$_2$ (Figure S17e,f, Supporting Information) and $Cu_3$(HCl-HH-*c*HBC)$_2$ (Figure S24e,f, Supporting Information) suggested the presence of exclusively $Cu^{2+}$ species, whereas $Cu_3$(HBr-HH-*c*HBC)$_2$ exhibited a $Cu^{2+}/Cu^{1+}$ ratio of 9:1, that could be estimated through deconvolution of the corresponding HR-spectra (Figure S30e,f, Supporting Information). Additionally, EDX-spectroscopy confirmed a uniform distribution of all expected elements (Figures S15, S27, and S29, Supporting Information).

Thermal stability measurements were conducted using the thermogravimetric analysis (TGA) method. $Cu_3$(HF-HH-*c*HBC)$_2$ and –(HCl-) showed similar stabilities (Figures S19 and S26, Sup-

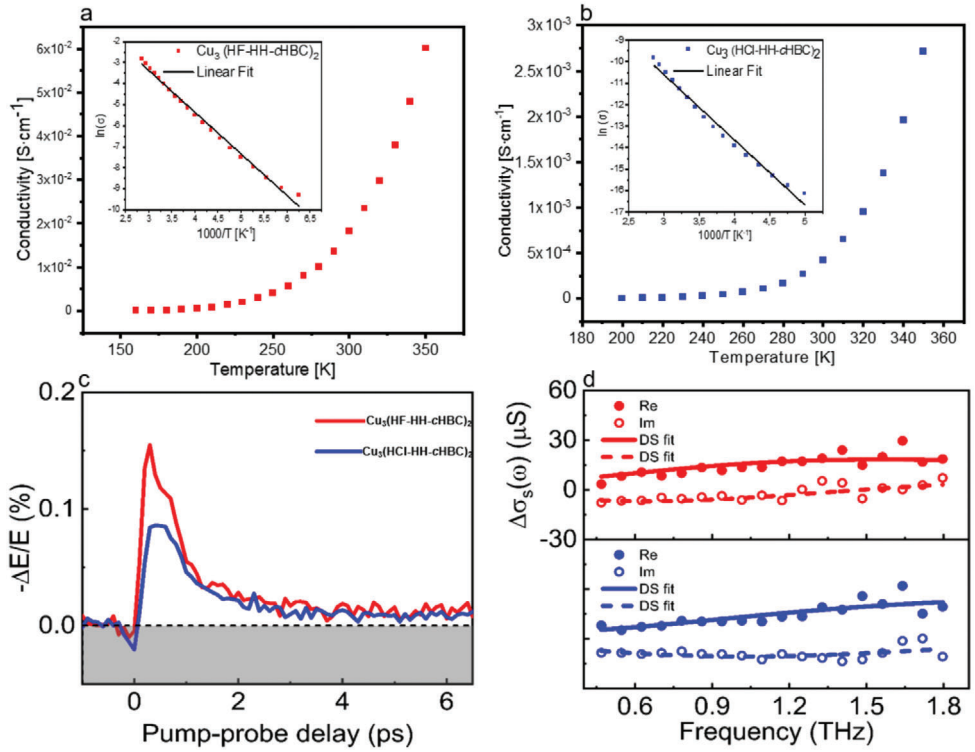


**Figure 4.** Electrical conductivity and THz mobility measurements of wavy 2D c-MOFs. a,b) Four-probe van der Pauw measurements of $Cu_3$(HF-HH-*c*HBC)$_2$ and $Cu_3$(HCl-HH-*c*HBC)$_2$ under vacuum with temperature, respectively. Inset: the linear fit of the conductivity measurements. c) Terahertz measurements of $Cu_3$(HF-HH-*c*HBC)$_2$ and $Cu_3$(HCl-HH-*c*HBC)$_2$, respectively. d) According to the Drude-Smith model, charge carrier mobilities were calculated: 9.3 ± 1.1 cm$^2$ (V s)$^{-1}$ for $Cu_3$(HF-HH-*c*HBC)$_2$ and 3.3 ± 0.4 cm$^2$ (V s)$^{-1}$ for $Cu_3$(HCl-HH-*c*HBC)$_2$.

porting Information) with an approximated loss of weight of 5% upon reaching 300 °C, respectively. $Cu_3$(HBr-HH-*c*HBC)$_2$ exhibited lower stability, losing 5% of its weight at already 200 °C (Figure S32, Supporting Information). These results are congruent with the already discussed crystallinity and morphology. We tested the stability of the three MOFs through dispersion of them in organic solvents, such as DCM, acetone, DMF, and ethanol, as well as 1 M aqueous HCl- and NaOH- solutions for three days, at ambient temperature. Overall, the three MOFs were stable in these utilized organic solvents, as evidenced through PXRD measurements (Figures S33–S35, Supporting Information). In contrast, $Cu_3$(HF-HH-*c*HBC)$_2$ and $Cu_3$(HCl-HH-*c*HBC)$_2$ could retain their structural integrity in the HCl solution, whereas $Cu_3$(HBr-HH-*c*HBC)$_2$ was dissolved completely under the same conditions. In addition, all three MOFs could be dissolved in NaOH solution.

Next, we investigated the electrical conductivity of all three MOFs as pellet samples, using the four-probe van der Pauw measurements under vacuum. The determined electrical conductivities were 1.82 × 10$^{-2}$ S cm$^{-1}$ and 4.26 × 10$^{-4}$ S cm$^{-1}$ for -(HF-) and $Cu_3$(HCl-HH-*c*HBC)$_2$ at room temperature, respectively (Figure 4a,b). For $Cu_3$(HBr-HH-*c*HBC)$_2$ the prepared pellets were too fragile and upon measuring the resistance was too high to determine the electrical conductivity. These results are in good agreement with the crystallinity and morphology of all three MOFs. The temperature-dependent linear fits (**Figure** 4a,b) suggested semiconductive behavior for -(HF-) and $Cu_3$(HCl-HH-*c*HBC)$_2$. Through the Arrhenius plot, the activation energies of $E_{a,HF}$ = 0.34 eV, $E_{a,HCl}$ = 0.52 eV were determined. Again, these results correlate very well with the degree of crystallinity and morphology. Furthermore, the charge carrier properties were characterized using time-resolved terahertz spectroscopy (THz). Following the photogeneration of charge carriers in the samples excited by a 400 nm ultrashort laser pulse, the transport properties were probed by a freely propagating THz pulse. The pump-induced relative attenuation of the THz field is proportional to the photoconductivity.[26] As shown in Figure 4c, -(HF-) and $Cu_3$(HCl-HH-*c*HBC)$_2$ exhibited a rapid rise in photoconductivity due to the photo injection of charge carriers. This was followed by a decay process on the picosecond timescale due to electron-hole recombination or exciton formation.[27] Describing the measured frequency-resolved photoconductivity by the Drude-Smith model[28] (see Supporting Information) yields an average scattering time of $(\tau)_{HF}$: 96 ± 11 fs for $Cu_3$(HF-HH-*c*HBC)$_2$ and $(\tau)_{HCl}$: 62 ± 7 fs for $Cu_3$(HF-HH-*c*HBC)$_2$ (Figure 4d). Assuming $m^* = m_0$, we estimate their charge carrier mobilities in the DC-limit to be $\mu_{HF}$ = 9.3 ± 1.1 cm$^2$ (V s)$^{-1}$ for $Cu_3$(HF-HH-*c*HBC)$_2$ and 3.3 ± 0.4 cm$^2$ (V s)$^{-1}$ for $Cu_3$(HCl-HH-*c*HBC)$_2$.

Based on the experimental results of the optical absorption, electrical conductivity characterizations, and THz results, we suggest a semiconductive behavior for $Cu_3$(HF-HH-cHBC)$_2$ and –(HCl-). The band structure of $Cu_3$(HF-HH-cHBC)$_2$ with missing ions is displayed in **Figure** 5. While the band structure of a defect-free single crystal can be considered metallic, there is

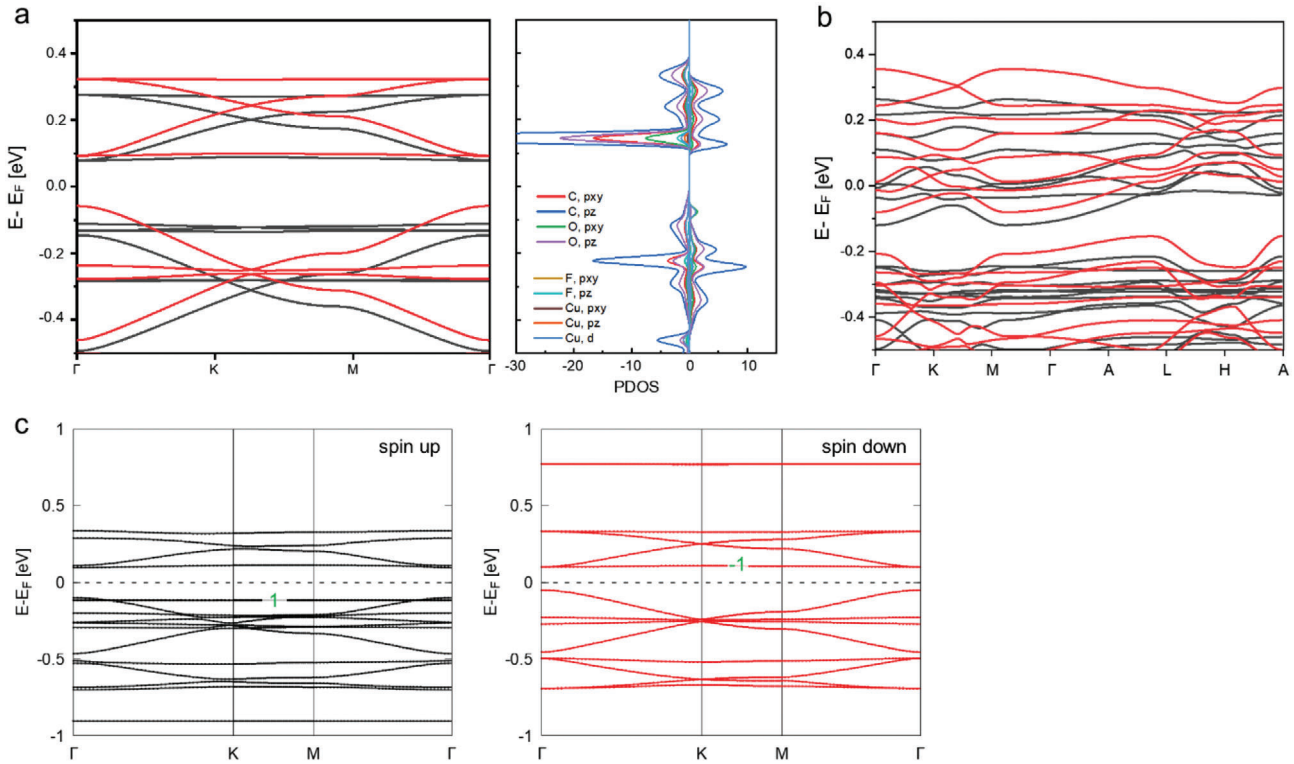


**Figure 5.** Electronic structures of $Cu_3$(HF-HH-*c*HBC)$_2$. a) Monolayer and b) staggered AA stacking models, respectively, with spin-up (black) and spin-down (red) states. c) The Wannier interpolated band structure. The dashed black line denotes the Fermi level. Spin-up and spin-down densities of states do not overlap, indicating the presence of spin polarization in the structures.

a small gap under the fermi level, so that defects with several (one/two) missing ions per unit cell are expected to be relatively stable. When such defects are present, a bandgap is expected to be opened at the fermi level (Figure 5). The monolayer and AA-shift structures are considered with 2 electrons and 4 electrons missing. It shows a bandgap of 0.14 eV for the monolayer structure and 0.10 eV for the AA-shift bulk structure, showing good agreement with the experimental results, further validating the predicted semiconductive behavior. [29–33] The partial density of states (PDOS) shows that the bands are mainly contributed by the $p_z$ orbital of C, with O $p_z$, C $p_{xy}$, and $O_{xy}$ making smaller contributions (Figure 5a; Figure S36 and S37, Supporting Information). There are two flat bands near the Fermi level, separated by a gap, with opposite Chern number (Figure 5c). This feature was reported as "yin-yang", which has the potential for exotic many-body quantum phenomena, as indicated by the references to the excitonic insulator and exciton Bose–Einstein condensation.[34,35]

As a proof-of-concept, we further evaluated the aluminum-ion storage performance of $Cu_3$(HF-HH-*c*HBC)$_2$ as cathode material in a three-electrode system using urea as an electrolyte. The cyclic voltammetry and galvanostatic charge–discharge (GCD) curves reveal an average capacity of 148 mAh $g^{-1}$ for $Cu_3$(HF-HH-cHBC)$_2$ at a current of 0.1 A $g^{-1}$ and an average voltage of 1 V, which shows potential applications in hybrid supercapacitors and aluminum-ion batteries (Figure S38a, Supporting Information). Additionally, the $Cu_3$(HF-HH-cHBC)$_2$ electrode also presents certain cycling stability. After 300 cycles of charge/discharge process at 100 mA $g^{-1}$, the average capacity of 2D c-MOF could retain 92 mAh $g^{-1}$ (Figure S38b, Supporting Information).

## 3. Conclusion and Outlook

In conclusion, we designed and synthesized a novel class of organic building blocks by introducing the *c*-HBC-ligand as a new member of the reported MOF systems. Due to its short and flexible synthetic route, the *c*-HBC ligand allows a vast variety of substitution patterns, including the incorporation of electron-withdrawing groups that can be used to fine-tune the properties in a controlled manner. We used this possibility to investigate systematically the effect of EWG on the properties of the resulting MOF-materials and discovered, that the incorporation of fluorine, as strong EWG, is a powerful method to enhance the crystallinity, electrical conductivity as well as charge carrier mobility and porosity. These beneficial features were not so much attributed to an electron-poor core, but rather to favorable steric interactions along the c-axis that apparently play a key role during the crystal growth phase. These insights shed new light on the still limited understanding of the structure-property relationship and provide future researchers with a powerful design strategy.

## Supporting Information

Supporting Information is available from the Wiley Online Library or from the author.

## Acknowledgements

K.J. and Y.Z. contributed equally to this work. This work was financially supported by the ERC starting grant (FC2DMOF, No. 852909), DFG projects (CRC-1415, No. 417590517; GRK-2861, No. 491865171), as well as the German Science Council and Center for Advancing Electronics Dresden (CFAED). R.D. thanks Taishan Scholars Program of Shandong Province (tsqn201909047), the Natural Science Foundation of Shandong Province (ZR2023JQ005) and the National Natural Science Foundation of China (22272092). The authors acknowledge the use of the facilities at the Dresden Center for Nanoanalysis at Technische Universität Dresden. The authors thank the Center for Information Services and High-Performance Computing (ZIH) at TU Dresden for generous allocations of computer time. Furthermore, Y.Z. acknowledges China Scholarship Council and M.P. thanks the Saxonian Ministry for Science and Art (DCC F-012177-701-XD0-1030602) and EMPIR-20FUN03-COMET for supporting fundings.

Open access funding enabled and organized by Projekt DEAL.

## Conflict of Interest

The authors declare no conflict of interest.

## Data Availability Statement

The data that support the findings of this study are available from the corresponding author upon reasonable request.

## Keywords

2D conjugated MOFs, conductive MOFs, halogen substitution, tunable crystallinity, wavy structure

Received: August 6, 2023
Revised: November 16, 2023
Published online: December 11, 2023

[1] M. Hmadeh, Z. Lu, Z. Liu, F. Gándara, H. Furukawa, S. Wan, V. Augustyn, R. Chang, L. Liao, F. Zhou, E. Perre, V. Ozolins, K. Suenaga, X. Duan, B. Dunn, Y. Yamamto, O. Terasaki, O. M. Yaghi, *Chem. Mater.* **2012**, *24*, 3511.
[2] M. Ko, L. Mendecki, K. A. Mirica, *Chem. Commun.* **2018**, *54*, 7873.
[3] Z. Meng, R. M. Stolz, L. Mendecki, K. A. Mirica, *Chem. Rev.* **2019**, *119*, 478.
[4] L. S. Xie, G. Skorupskii, M. Dinca, *Chem. Rev.* **2020**, *120*, 8536.
[5] W.-T. Koo, J.-S. Jang, I.-D. Kim, *Chem* **2019**, *5*, 1938.
[6] M. G. Campbell, M. Dincă, *Sensors* **2017**, *5*, 17.
[7] I. Stassen, N. Burtch, A. Talin, P. Falcaro, M. Allendorf, R. Ameloot, *Chem. Soc. Rev.* **2017**, *46*, 3185.
[8] K. W. Nam, S. S. Park, R. Reis, V. P. Dravid, H. Kim, C. A. Mirkin, J. F. Stoddart, *Nat Commun* **2019**, *10*, 4948.
[9] K. Wada, K. Sakaushi, S. Sasaki, H. Nishihara, *Angew. Chem., Int. Ed.* **2018**, *57*, 8886.
[10] E. Pomerantseva, F. Bonaccorso, X. Feng, Y. Cui, Y. Gogotsi, *Science* **2019**, *366*, 6468.
[11] E. M. Miner, T. Fukushima, D. Sheberla, L. Sun, Y. Surendranath, M. Dinca, *Nat Commun* **2016**, *7*, 10942.
[12] X. Huang, P. Sheng, Z. Tu, F. Zhang, J. Wang, H. Geng, Y. Zou, C.-A. Di, Y. Yi, Y. Sun, W. Xu, D. Zhu, *Nat. Commun.* **2015**, *6*, 7408.
[13] T. Kambe, R. Sakamoto, K. Hoshiko, K. Takada, M. Miyachi, J.-H. Ryu, S. Sasaki, J. Kim, K. Nakazato, M. Takata, H. Nishihara, *J. Am. Chem. Soc.* **2013**, *135*, 2462.
[14] A. J. Clough, J. W. Yoo, M. H. Mecklenburg, S. C. Marinescu, *J. Am. Chem. Soc.* **2015**, *137*, 118.
[15] J.-H. Dou, L. Sun, Y. Ge, W. Li, C. H. Hendon, J. Li, S. Gul, J. Yano, E. A. Stach, M. Dinca, *J. Am. Chem. Soc.* **2017**, *139*, 13608.
[16] J. Park, A. C. Hinckley, Z. Huang, D. Feng, A. A. Yakovenko, M. Lee, S. Chen, X. Zou, Z. Bao, *J. Am. Chem. Soc.* **2018**, *140*, 14533.
[17] L. Sun, M. G. Campbell, M. Dinca, *Angew. Chem., Int. Ed.* **2016**, *55*, 3566.
[18] Z. Meng, K. A. Mirica, *Nano Res.* **2021**, *14*, 369.
[19] R. Dong, Z. Zhang, D. C. Tranca, S. Zhou, M. Wang, P. Adler, Z. Liao, F. Liu, Y. Sun, W. Shi, Z. Zhang, E. Zschech, S. C. B. Mannsfeld, C. Felser, X. Feng, *Nat. Commun.* **2018**, *9*, 2637.
[20] M. Wang, H. Shi, P. Zhang, Z. Liao, M. Wang, H. Zhong, F. Schwotzer, A. S. Nia, E. Zschech, S. Zhou, S. Kaskel, R. Dong, X. Feng, *Adv. Funct. Mater.* **2020**, *30*, 2002664.
[21] J.-H. Dou, M. Q. Arguilla, Y. Luo, J. Li, W. Zhang, L. Sun, J. L. Mancuso, L. Yang, T. Chen, L. R. Parent, G. Skorupskii, N. J. Libretto, C. Sun, M. C. Yang, P. V. Dip, E. J. Brignole, J. T. Miller, J. Kong, C. H. Hendon, J. Sun, M. Dinca, *Nat. Mater.* **2021**, *20*, 222.
[22] M. Martínez-Abadía, C. T. Stoppiello, K. Strutynski, B. Lerma-Berlanga, C. Martí-Gastaldo, A. Saeki, M. Melle-Franco, A. N. Khlobystov, A. Mateo-Alonso, *J. Am. Chem. Soc.* **2019**, *141*, 14403.
[23] G. Xing, J. Liu, Y. Zhou, S. Fu, J.-J. Zheng, X. Su, X. Gao, O. Terasaki, M. Bonn, H. I. Wang, L. Chen, *J. Am. Chem. Soc.* **2023**, *145*, 8979.
[24] Q. Zhang, H. Peng, G. Zhang, Q. Lu, J. Chang, Y. Dong, X. Shi, J. Wei, *J. Am. Chem. Soc.* **2014**, *136*, 5057.
[25] P. Pyykkö, M. Atsumi, *Chem. Eu. J.* **2008**, *15*, 186.
[26] V. Blum, R. Gehrke, F. Hanke, P. Havu, V. Havu, X. Ren, K. Reuter, M. Scheffler, *Com. Phys. Commun.* **2009**, *180*, 2175.
[27] J. P. Perdew, K. Burke, M. Ernzerhof, *Phys. Rev. Lett.* **1996**, *77*, 3865.
[28] A. Tkatchenko, M. Scheffler, *Phys. Rev. Lett.* **2009**, *102*, 073005.
[29] R. Ulbricht, E. Hendry, J. Shan, T. F. Heinz, M. Bonn, *Rev. Mod. Phys.* **2011**, *83*, 543.
[30] A. Tries, S. Osella, P. Zhang, F. Xu, C. Ramanan, M. Kläui, Y. Mai, D. Beljonne, H. I. Wang, *Nano Lett.* **2020**, *20*, 2993.
[31] T. L. Cocker, D. Baillie, M. Buruma, L. V. Titova, R. D. Sydora, F. Marsiglio, F. A. Hegmann, *Phys. Rev. B* **2017**, *96*, 205439.
[32] Z. Liu, Z.-F. Wang, J.-W. Mei, Y.-S. Wu, F. Liu, *Phys. Rev. Lett.* **2013**, *110*, 106804.
[33] W. Jiang, X. Ni, F. Liu, *Acc. Chem. Res.* **2021**, *54*, 416.
[34] G. Sethi, Y. Zhou, L. Zhu, L. Yang, F. Liu, *Phys. Rev. Lett.* **2021**, *126*, 196403.
[35] G. Sethi, M. Cuma, F. Liu, *Phys. Rev. Lett.* **2023**, *130*, 186401.